scientific reports

Check for updates

OPEN

Absorption cross section of gold nanoparticles based on NIR laser heating and thermodynamic calculations

Mazen Alrahili[1,3]✉, Viktoriia Savchuk[1], Kelly McNear[2] & Anatoliy Pinchuk[1,2]

We present a method for measuring the optical absorption cross section (σ_{abs}) of gold nanoparticles (GNPs) based on optically heating the solution of GNPs with an 808 nm near-infrared (NIR) laser and measuring the temperature increase of the solution. We rely on the theoretical calculations based on the heat diffusion equations and experimental measurements based on the energy balance equations to measure the σ_{abs} and the temperature distribution of single GNPs. Several morphologies, including gold nanospheres (GNSs), spherical gold nanoparticle conjugate (AuNPC), which are 20 nm GNSs surface-functionalized with an IR 808 dye, gold nanorods (GNRs), and gold nanourchins (GNUs), were studied. The study found that a single 20 nm GNS has the lowest σ_{abs} and temperature distribution as compared to 100 nm GNUs. By increasing the size of GNSs from 20 to 30 nm, the magnitude of σ_{abs} as well as temperature distribution increases by a factor of 5. The σ_{abs} values of 20 and 30 nm GNSs calculated by Mie theory and the experimentally measured are in a good agreement. GNRs with equivalent radius (R_{eq}) 9.16 nm show the second lowest σ_{abs}. By increasing the R_{eq} by a factor of 2 to 19.2 nm, the measured σ_{abs} and temperature distribution also increased by a factor of 2. We also estimated σ_{abs} for GNUs with diameters at 80 and 100 nm, which also have higher σ_{abs} values. This work confirms that we can use temperature to accurately measure the σ_{abs} of a variety of GNPs in solution.

The remarkable optical properties of GNPs have captured a lot of attention over the last few decades due to a broad range of applications as varied as imaging, sensing, gene and drug delivery, and more recently, biomedical applications such as hyperthermia using near-infrared (NIR) light[1–5]. NIR light is often used since biological tissues such as skin have low absorption and high penetration in the first and second biological windows—700–900 nm and 1000–1700 nm, respectively[6–11]. GNPs can be developed in different morphologies such as nanospheres, nanorods, nanoshells, nanourchins, and more. Depending on the shapes and sizes, the surface plasmon resonance (SPR) can be over a wide spectrum from visible to NIR region[12,13]. For instance, GNSs have SPR in the visible region and GNRs have strong SPR in the NIR region. A methodology for synthesizing GNPs has been a challenging task in the scientific community. Therefore, different methods have been used to develop many morphologies. The best chemical method to achieve the enlarging demand of GNPs is well-known as the citrate reduction method due to many advantages including inexpensive reductant, water solvent, and non-toxic[14]. Other chemical methods can be found and described in the literature[15–18].

Typically, optical losses in plasmonic nanoparticles (NPs) are considered to be an obstacle for applications such as plasmonic optical waveguides. However, for hyperthermia applications, optical losses are beneficial since GNPs can be used as local sources of heat conversion from light into thermal energy. Recently, we investigated a set of nano-gold with different morphologies such as GNSs, GNRs, GNUs, and gold conjugates with IR dye attached to 20-nm GNSs. We found that AuNPC exhibit an enhanced 'light to heat energy conversion efficiency (η)' by a factor four than those in the unmodified gold nanospheres[19].

It is important to know the η-value as a function of a laser power density for optimizing the hyperthermia procedure as well as an efficient light source that can be used in its applications. The results can be extended to calculate the rise in the local temperature, δT_h, per single NP of different shapes, which can be useful in

[1]Department of Physics and Energy Science, University of Colorado Colorado Springs, 1420 Austin Bluffs Parkway, Colorado Springs, CO 80918, USA. [2]UCCS BioFrontiers Center, University of Colorado Colorado Springs, 1420 Austin Bluffs Parkway, Colorado Springs, CO 80918, USA. [3]Physics Department, School of Science, Taibah University, Janadah Bin Umayyah Road, Medina 42353, Saudi Arabia. ✉email: mrahili@taibahu.edu.sa

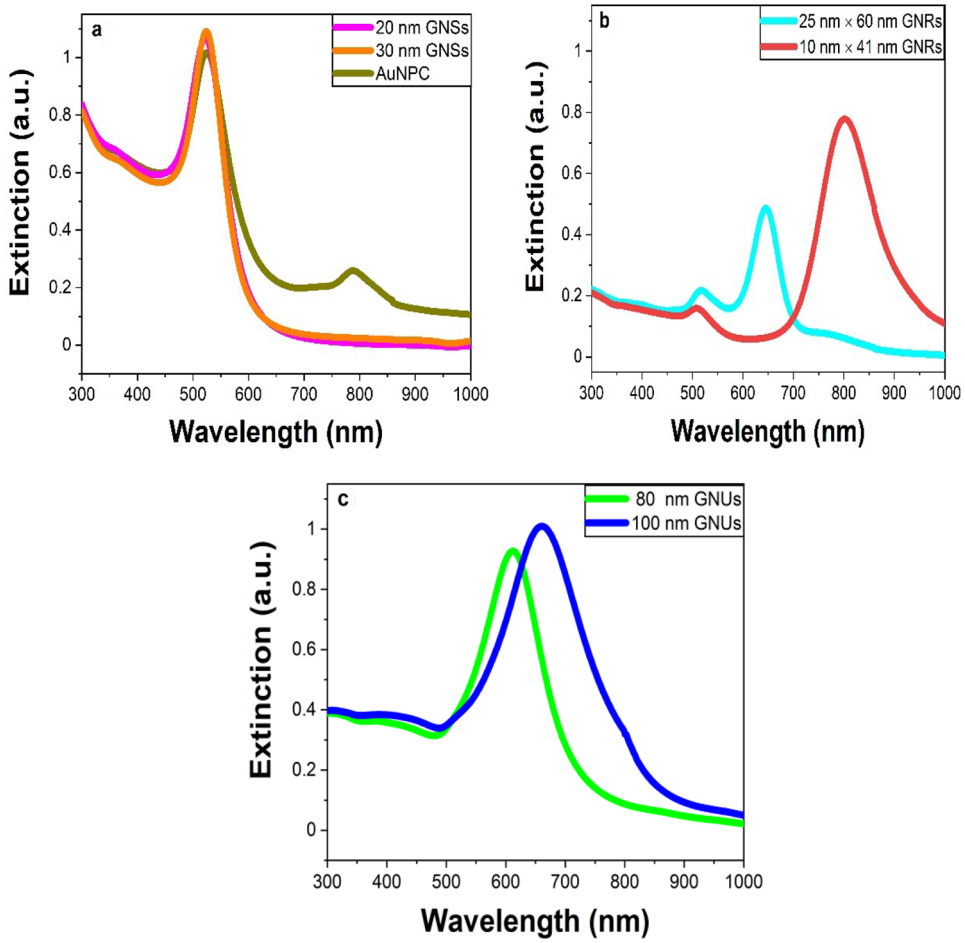

Figure 1. The extinction spectra of the different nanogold samples of (**a**) 20 and 30 diameters GNSs, (**b**) 25 and 10 diameters GNRs and (**c**) 80 and 100 nm diameters GNUs. All solutions were measured at a normalized optical density (OD) 1.

translating potential candidates for photothermal therapy from benchtop to clinic. Furthermore, one can use the δT value to calculate σ_{abs} in the selected particle. The σ_{abs} of colloidal GNPs can be experimentally measured by using a UV–Vis absorption spectrophotometer[20]. One can also calculate the optical absorption (or extinction) cross section of the NPs by using Mie theory[21]. Typically, the experimental and theoretical results for the σ_{abs} agree well for GNSs of different sizes. For non-spherical NPs, numerical methods such as Discrete Dipole Approximation (DDA) can be used to calculate their σ_{abs} values[22]. It is interesting to know if the σ_{abs} measured by using an optical spectrometer, or calculated by Mie theory, matches the values extracted from temperature measurements in hyperthermia-type or thermo-plasmonic type experiments.

In this article, we estimated the σ_{abs} values of nanogold of a variety of nontrivial morphologies dispersed in a liquid host after selective dosages of NIR irradiations. This is done by measuring the temperature rise of nanogold in the solution when exposed to a continuous laser of an 808 nm wavelength at varying power densities and then averaging the value per particle. The obtained σ_{abs} is compared to the calculated value in the Mie theory. It is found that the σ_{abs} value sensitively varies in the samples of varied morphologies consistently to the calculated values. This opens a door for developing a basic understanding of the fundamental properties of nanogold of complex morphologies.

Results

Optical extinction spectra of nanogold of different morphologies. Here, seven different types of nanogold with various sizes were studied, including 20 and 30 nm GNSs, 20 nm core AuNPC, 80 and 100 nm GNUs, and 25 nm × 60 nm and 10 nm × 41 nm GNRs. Figure 1a shows the extinction spectra of the SPR bands obtained for these samples. 20 nm and 30 nm GNSs exhibit an intense SPR band in the visible region with a peak position at 520 nm. As mentioned above, the AuNPC sample, which is a surface-functionalized sample of 20 nm GNSs with an IR 808 dye, exhibits a strong SPR band at 520 nm with a weak satellite band at 788 nm (from the dye). In 80 nm GNUs, the SPR band is displaced at 620 nm, which is shifted to 680 nm on raising their average size to 100 nm. Further, 25 nm × 60 nm and 10 nm × 41 nm GNRs, having different diameters of 25 nm and 10 nm, respectively, exhibit two well-known SPR bands of transverse and longitudinal modes of the plasmons[7,10].

The SPR bands we observed here are very much consistent to those reported in different shapes of nanogold as given in Table S1 in the supporting information.

Heating temperature profile of nanogold samples. Seven colloidal suspensions of the nanogold samples were optically heated by the NIR laser at different power densities of 0.3, 1.2, 2.5, and 5.1 W/cm^2. During laser irradiation, the nanogold absorbs part of the light which it then converts into thermal energy, which transfers to the surrounding medium. As shown in Fig. 2, the highest temperature elevation was thus observed for the 10 nm × 41 nm GNRs, with the second most value found in the 100 nm GNUs. The results confirm that the GNRs and GNUs conduct usefully larger temperature rise than the spheroids of the same volume. This heat increase is well-supported with the literature[23–25]. A value δT = 60 °C is found for the 10 nm × 41 nm GNRs in which the SPR band overlaps the laser signal and that is dropped to 35 °C in the 100 nm GNUs. In all cases, δT_h follows the same trend at all four power densities. The larger laser power used the larger δT_h value induced in the present samples.

Temperature increase by a single nanoparticle. To describe the local temperature profile inside and around nanogold dispersed in a solution, we use a heat transfer equation[26],

$$\rho C_p \frac{\partial T(\boldsymbol{r})}{\partial t} = \nabla \cdot [\kappa \nabla T(\boldsymbol{r})] + q(\boldsymbol{r}), \tag{1}$$

where ρ is the density of the medium of thermal conductivity (κ) and specific-heat-capacity (C_p) at constant pressure, and $T(\boldsymbol{r})$ is the absolute local temperature. In the steady-state regime, when the local temperature reaches its equilibrium profile, i.e. $\frac{\partial T(\boldsymbol{r})}{\partial t} = 0$, this equation reduces to,

$$\nabla \cdot [\kappa \nabla T(\boldsymbol{r})] = -q(\mathbf{r}). \tag{2}$$

Assuming k-values for gold and water as $\kappa_g = 318$ W m^{-1}K^{-1} and $\kappa_w = 0.6$ W m^{-1}K^{-1} respectively, Eq. (2) can be split into two parts;

$$\kappa_g \nabla^2 \mathrm{T}(\boldsymbol{r}) = -q(\boldsymbol{r}), \quad \text{inside the nanogold} \tag{3}$$

$$\text{and} \quad \kappa_w \nabla^2 \mathrm{T}(\boldsymbol{r}) = 0, \quad \text{outside the nanogold.} \tag{4}$$

Mathematically, Eqs. (3) and (4) are equivalent to Poisson's and Laplace's equations in electrostatics, where T is equivalent to the electrostatic potential, κ is equivalent to dielectric permittivity, and $q(\boldsymbol{r})$ is equivalent to local charge density[27]. Using the analogy with electrostatics, we can find their solutions of the second-order differential equations and write $\delta \mathrm{T}_{NP}(\boldsymbol{r})$ for a GNS of radius R as,

$$\delta \mathrm{T}_{NP}(\boldsymbol{r}) = \frac{P}{4\pi \kappa_w r}, \quad \text{for r} > \mathrm{R} \tag{5}$$

and

$$\delta \mathrm{T}_{NP}(\boldsymbol{r}) = \frac{P}{4\pi R \kappa_g}, \quad \text{for r} < \mathrm{R}, \tag{6}$$

where P is the total electromagnetic power absorbed by the nanogold, which can be calculated as;

$$P = \int q(\boldsymbol{r}) d\boldsymbol{r} = \sigma_{abs} I, \tag{7}$$

where I is the power density of the incoming electromagnetic signal integrated over the surface of a spheroid. For a non-spherical morphology, thus one can rewrite an expression[27],

$$\frac{P}{\delta T_{NP} = 4R_{eq}\beta\kappa_{gold}} = \frac{\sigma_{abs} I}{4R_{eq}\beta\kappa_{gold}} \tag{8}$$

where R_{eq} is the equivalent NP radius of a volume V equal to that of a spheroid, i.e.[28,29],

$$R_{eq} = \left(\frac{3V}{4}\right)^{1/3} \tag{9}$$

An average β value for nanorods can be given by the following expression[30],

$$\beta = 1 + 0.96587 ln^2\left(\frac{h}{d}\right), \tag{10}$$

where h is the length of the GNRs of diameter d. In simplifying the calculations, we consider only the core diameter and ignore contribution from the dye for AuNPC and sharp branches for GNUs. Hence, both have the same (β) 1 thermal capacitance geometrical correction factor (dimensionless).

As mentioned above, when heated by laser irradiation, the colloidal sample will reach equilibrium, $\frac{\partial T(\boldsymbol{r})}{\partial t} = 0$. For example, Fig. 2a plots the δT values obtained as a function of the laser power density for the nanogold samples of different shapes. To find an average value per particle, one needs to determine GNPs present per unit volume,

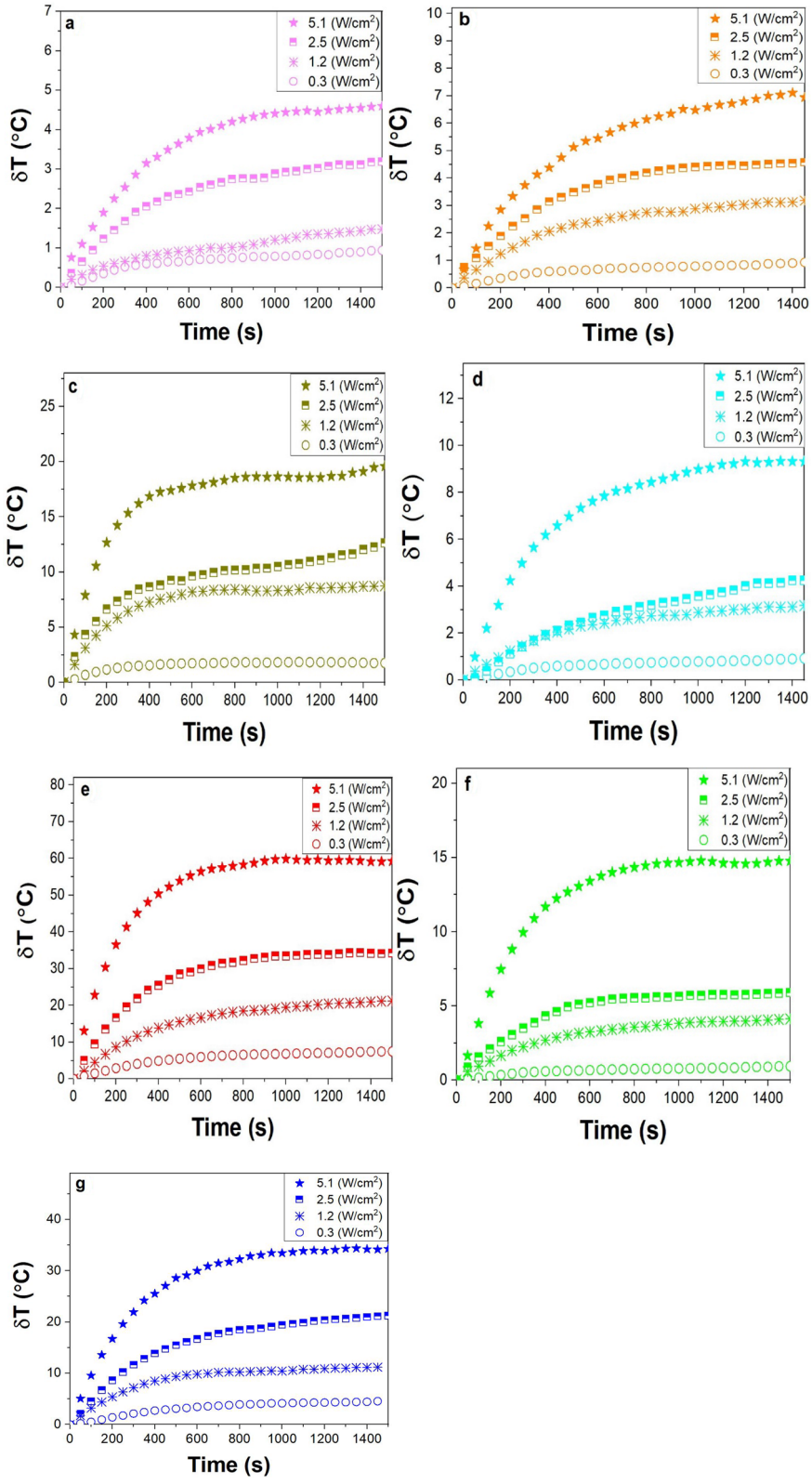

Figure 2. The evolution of δT as a function of irradiation time (s) for (**a**) 20 nm GNSs, (**b**) 30 nm GNSs, (**c**) AuNPC, (**d**) 25 nm × 60 nm GNRs, (**e**) 10 nm × 41 nm GNRs (**f**) 80 nm GNUs, and (**g**) 100 nm GNUs. All the solutions were measured over 25 min of irradiation by the CW NIR laser of densities of 0.3, 1.2, 2.5, and 5.1 W/cm^2. All solutions were excited at OD = 1.

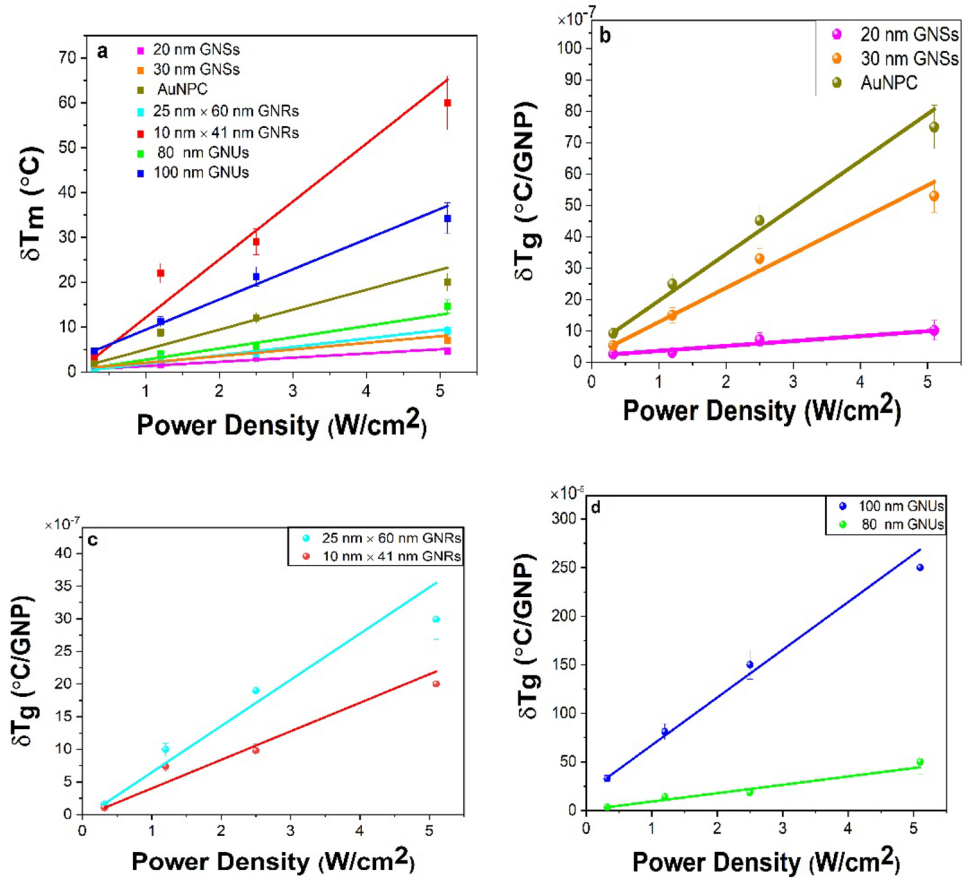

Figure 3. Temperature elevation in the colloidal solutions as a function of power density; (**a**) the net values on different GNPs in the solutions after subtracting the background, with average values per single GNPs for (**b**) 20 nm and 30 nm GNSs and AuNPC, (**c**) 25 nm × 60 nm and 10 nm × 41 nm GNRs, and (**d**) 80 nm and 100 nm GNUs.

i.e., N_g per mL, in the sample. In this experiment, we used 3 mL of the GNP solution. It can be expressed at the equilibrium as follows,

$$\delta T_s = \frac{\delta Tm}{N}. \tag{11}$$

Here, δT_s is the saturation temperature (°C) obtained per single particle following a net δT_m value in Fig. 2 at the equilibrium and then graphed in Fig. 3a as a function of power density. In the experimental conditions, $N = N_g V_s$, as can be seen in Table S1 in the supporting information, and V_s is the sample volume. It should also be noted that since the above equation determines the temperature distribution by a single GNP in solution, we need to solve the energy balance equation of the system in order to determine the temperature change of the entire solution. The energy balance of the system of temperature conservation changes in a solution due to GNPs can be written as follows[31,32],

$$\sum_i m_i C_i \frac{dT}{dt} = Q_{in} - Q_{out}, \tag{12}$$

where m_i *and* C_i are the mass and the specific heat of the components, respectively. Q_{in} is the input heat (incident light) and Q_{out} is the output heat dissipated in the surrounding medium. At the equilibrium position, $Q_{in} \cong Q_{out}$. Thus, the energy balance can be rewritten as,

$$m_S C_S \delta T_S = m_g C_g \delta T_g \tag{13}$$

where m_S and C_S are the mass and the specific heat of the solution and m_g, C_g, and δT_g are the mass, the specific heat, and the temperature change of the GNPs. Rearranging, we get

$$\delta T_g = \frac{m_S C_S}{m_g C_g} \delta T_S \tag{14}$$

The significance of Eq. (12) is that the mass in single GNPs plays a major role in the net temperature change. In different nanogold morphologies studied here, all the parameters are constant except for m_g which varies depending on the size of the GNPs as given in Table S1. For each type of nanogold, the temperature change in the solution was calculated and reported in Table S2. It should be noted that δT_S is calculated using Eq. (9), while δTm is measured from the experiments at the equilibrium as shown in Fig. 3a.

Absorption cross section of nanogold of different morphologies. To estimate the temperature distribution of single GNPs, one must rely on the theoretical calculations and experimental measurements to determine the σ_{abs} value, i.e. written from Eq. (5) as,

$$\sigma_{abs}\left(\mathrm{m}^2\right) = \frac{\delta T_g}{I} 4\mathrm{R}\kappa_w = \Phi 4\mathrm{R}\kappa_w \tag{15}$$

For a non-spherical nanomaterial, it can be expressed after Eq. (8) as,

$$\sigma_{abs}\left(\mathrm{m}^2\right) = \frac{\delta T_g}{I} 4R_{eq}\beta\kappa_w \cong \Phi 4R_{eq}\beta\kappa_w, \tag{16}$$

where Φ is the slope, °C *m^2/W, as can be extracted from the plots in Fig. 3b–d, with $\delta T_{NP}(\boldsymbol{r}) \cong \delta T_g$. The experimental σ_{abs} per particle is presented in Table S3 after subtracting the background, as plotted in Fig. S1. A similar value is obtained by feeding the experimental results in Eqs. (13) and (14). For spherical nanomaterials, 20 nm GNSs have a measured $\sigma_{abs} = (2.1 \pm 0.316) \times 10^{-18}$ m^2, which is enhanced to $(10.0 \pm 0.937) \times 10^{-18}$m^2 in the 30 nm GNSs.

In the case of GNRs, we obtained the experimental σ_{abs} values by feeding the experimental results into Eq. (14). Thus, 25 nm × 60 nm GNRs, having $R_{eq} = 19.2$ nm and $\beta = 1.74$, as determined by Eqs. (7) and (8), respectively, have $\sigma_{abs} = (16.2 \pm 1.676) \times 10^{-18}$ m^2. A bit smaller $\sigma_{abs} = (7.49 \pm 1.254) \times 10^{-18}$ m^2 persists in the sample of 10 nm × 41 nm GNRs with $R_{eq} = 9.16$ nm and $\beta = 2.92$. The same procedure yields $\sigma_{abs} = (25.5 \pm 4.084) \times 10^{-16}$ m^2 for 80 nm GNUs, which is promoted to $(18.4 \pm 1.216) \times 10^{-15}$m^2 on an increased core diameter to 100 nm.

Discussion

Eventually, a tailored σ_{abs}value, which is markedly varied in nanogold of its effective size is varied in three representative morphologies, viz., spheroids, rods, and urchins, displays five nontrivial effects of its (i) surface structure, (ii) local symmetry, (iii) charge carrier density of surface plasmons, (iv) polarization of surface charges, and (v) interactions (with the surroundings) on its optical properties in a nanocolloid (or a nanofluid) as follows. For example, an induced temperature in a sample of single 20 nm GNSs after laser irradiation (at a 5.1 W/cm^2 power) is found to be $\delta T_g = 1.02 \times 10^{-6}$ °C as seen in Fig. 3b in a model relation in Eq. (13), with $\sigma_{abs} = (2.1 \pm 0.316) \times 10^{-18} m^2$. When the diameter was increased to 30 nm, this value is increased nearly five times; with a final 5×10^{-6} °C value in the same conditions, due to prominent effects of the first four factors. Consistently, the σ_{abs} value is also increased by a similar factor, $\sigma_{abs} = (10.0 \pm 0.937) \times 10^{-18}$ m^2. A value of$\sigma_{abs} = 2.4 \times 10^{-18}$ m^2 is calculated by Mie theory for 20 nm GNSs, while 8.5×10^{-18} m^2 for 30 nm GNSs, very similar to the measured σ_{abs} values. Further, the AuNPC sample is especially noteworthy in regards to increasing the σ_{abs} because it not only has a larger hydrodynamic diameter—due to a surface functionalizing with dye molecules at the surfaces[11], but it also has an absorbance in resonance with the laser light used for the irradiation. As a result, it enhances the σ_{abs} value significantly over the unfunctionalized GNSs.

In GNRs of two different sizes of 10 nm × 41 nm and 25 nm × 60 nm, the SPR band is split into (i) transverse and (ii) longitudinal modes of oscillation of the surface plasmons[5,6]. In the extinction spectra Fig. 1b, the first mode lies at 524 nm of a rather weak band in both the samples, while the second band is displaced in a strong band at 808 nm in the first sample, which is blue shifted at 650 nm on a markedly smaller aspect ratio 2.4 in the other sample over that of 4.1 in the first sample. The first sample ($R_{eq} = 9.16$ nm) exhibits $\delta T_g = 1.7 \times 10^{-6}$ °C, with$\sigma_{abs} = (7.49 \pm 1.252) \times 10^{-18}$ m^2, which is promoted to 3.2×10^{-6} °C on an increased $R_{eq} = 19.2$ nm by a factor of 2.1, with a proportionally enhanced $\sigma_{abs} = (16.2 \pm 1.676) \times 10^{-18}$ m^2 in the other sample. Thus, R_{eq} plays a critical role in harvesting δT_g in correlation to the σ_{abs}value of GNRs. While the DDA is widely used for calculating σ_{abs} for an elongated material[7,8], here we were able to calculate it for GNRs using R_{eg} based on the Mie theory, i.e. quite compatible to the measured value in Fig. 4. A value of $\sigma_{abs} = 1.8 \times 10^{-18}$ m^2 is thus calculated against a measured $(7.49 \pm 1.254) \times 10^{-18}$ m^2 value for 10 nm × 41 nm GNRs, while $\sigma_{abs} = 18.43 \times 10^{-18}$ m^2 compared to the measured $(16.2 \pm 1.676) \times 10^{-18}$ m^{2}one for 25 nm × 60 nm GNRs, as given in Tables S3 and S4. Together, these results confirm that R_{eq} and β are two very important parameters to tailor and experimentally determine σ_{abs} for GNRs.

Uniquely, GNUs, which contain spikes, uneven bumps, and thorns at the edges in the form of a core–shell nanostructure, duly trigger the electromagnetic fields at the surface leading to a red shift in the SPR band in a broader band of a multiple green-to-red color over 480–850 nm wavelengths as seen in Fig. 1c in comparison to those in the GNSs, useful for solar-energy, biological cells and other applications[33,34]. $\delta T_g \cong 46.5 \times 10^{-5}$ °C, as found in a sample of 80 nm GNUs, with $\sigma_{abs} = (25.5 \pm 4.089) \times 10^{-16}$ m^2, is markedly enhanced to 248.5×10^{-5} °C in that of 100 nm GNUs of a concomitantly enhanced $\sigma_{abs} \cong (18.4.0 \pm 1.216) \times 10^{-15}$ m^2. Evidently, it is the unique surface that effectively enhances the functionalized charger carriers which, in turn, enhances the σ_{abs} and the δT_g in the GNUs in comparison to those in the smooth, spherical samples.

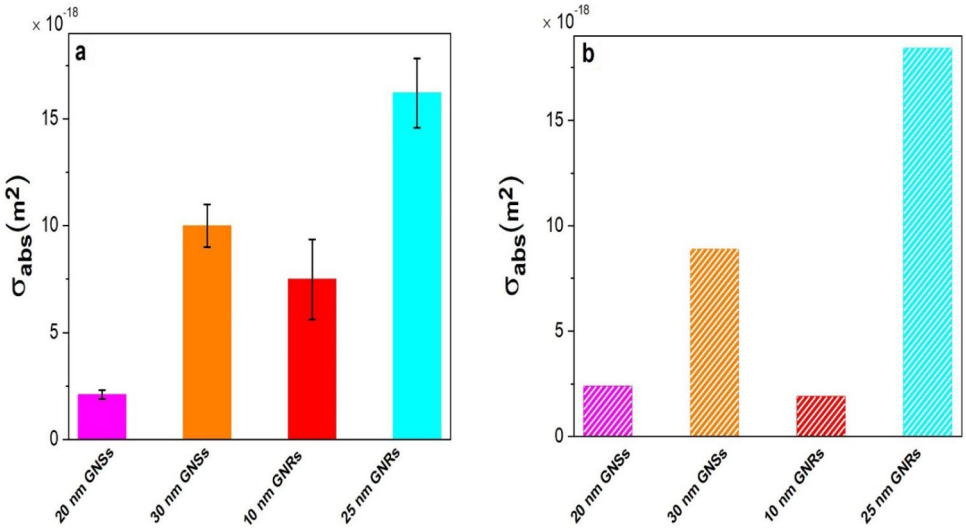

Figure 4. (**a**) Experimental σ_{abs} (based on thermodynamic theory) and (**b**) theoretical σ_{abs} (based on the Mie theory) for 20 nm and 30 nm GNSs, and 25 nm × 60 nm and 10 nm × 41 nm GNRs, wherein the error bars represent the standard deviation of triplicate measurements.

Conclusions

We demonstrate an analytical method for measuring the σ_{abs} value in terms of an induced temperature change of nanogold in a colloidal suspension (upon laser irradiation), based on the heat diffusion theory and energy balance of the system. An induced temperature in this experiment depends on primary factors of size, morphology, surface functionality of the nanogold, its exchange interaction with the surrounding, and the irradiation source of a given power density. The measured and calculated σ_{abs} values match closely for the GNS samples. Furthermore, when considering the SPR properties of light-absorption in NIR region of nanogold, the surface functionalization of 20 nm GNSs significantly improves the σ_{abs} value by a factor of more than 10. This method can be used to estimate the σ_{abs} of nanogold of complex shapes, such as nanorods and nanourchins. The results substantiate the nontrivial fact that GNUs promote the optical and thermal properties over GNSs and GNRs in an account of unique features of surface charge carriers. The results confirm that the optical cross section for a variety of nanomaterials can be determined by measuring the temperature change of the particles during laser irradiation and that this methodology can be extended to a variety of other materials. This approach can help develop our understanding of thermal properties of surface plasmonics by studying dynamics of laser induced heating of surface-charge-carriers in nanogold dispersed in a nanofluid in different functional structures.

Experimental methods

Chemical products. The samples of 10 nm × 41 nm and 25 nm × 60 nm GNRs, and 80 nm and 100 nm GNUs were purchased from Sigma-Aldrich (St. Louis, MO). 20 and 30 nm GNSs were purchased from Ted Pella (Redding, CA). GNPs functionalized with an IR 808 dye conjugate (AuNPCs) were chemically synthesized and supplied by Lahjavida (Colorado Springs, CO).

Experimental setup. The colloidal suspensions of nanogold (3 mL volume) were placed in a standard glass cuvette (VWR, Aurora, CO 80011), whose temperature was measured by using a thermocouple. All the solutions were studied at room temperature (23 °C) in which any induced temperature was recorded over 25 min of a CW NIR laser (808 nm) exposure, as shown in the schematic in Fig. 5. The temperature sensor was placed in the solution and not in the beam path as the scattering could lead to a non-zero response when aligning the beam, as seen in Fig. 5. A magnetic stir bar and plate, set to 300 rpm, were used to achieve uniform distribution of temperature, and a glass cuvette was used to avoid the reflection of the laser. While the cuvettes were not sealed, there was no solvent evaporation observed during the experimental measurements. The optical density (OD) of all solutions used were measured and normalized at 1. The NIR CW red laser beam of 808 nm wavelength and 4 W output power was used to determine the temperature profile of the samples. The laser power and the transmitted power were measured at a focused point by a digital power meter (PM100D, Thorlabs, Dachau, Germany). We used a half-wave plate (HWP) and a polarizing beam splitter (PBS) to adjust the power density of the beam over the sample.

Instrumentation. The extinction spectra of nanogold colloids were measured using a UV–VIS absorption spectrophotometer (Lambda 1050, PerkinElmer). A CW red laser of 4 W power was purchased from LaserLand (Wuhan Besram Technology, Hubei, China). The temperature was recorded using a temperature sensor (PS-2146, Pasco, Roseville, CA, US) in conjunction with PASCO Capstone software.

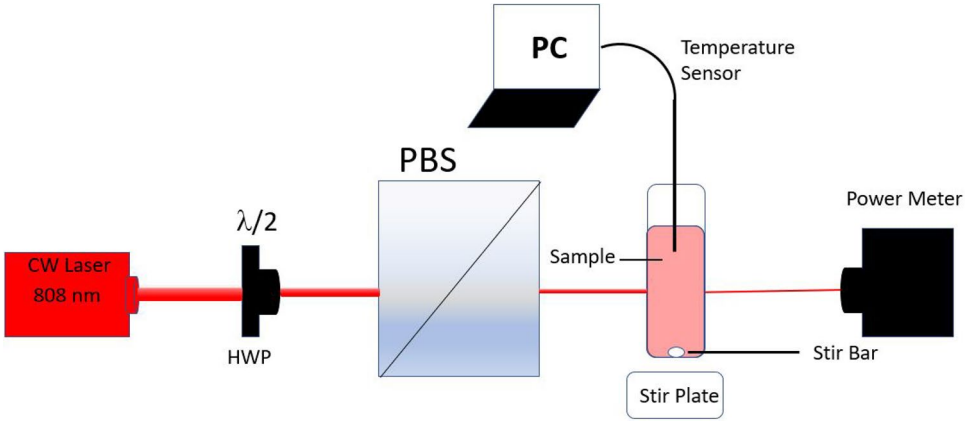

Figure 5. Experimental schematic for measuring temperature elevation in a nanocolloidal sample; HWP : a half-wave plate, PBS: a beam splitter, and PC: a computer.

Received: 26 July 2020; Accepted: 5 October 2020
Published online: 02 November 2020

References

1. Kato, H. *et al.* Imaging of thermal activation of actomyosin motors. *Proc. Natl. Acad. Sci.* **69**, 9602–9606 (1999).
2. Cognet, L. *et al.* Single metallic nanoparticle imaging for protein detection in cells. *Proc. Natl. Acad. Sci.* **100**, 11350–11355 (2003).
3. O'Neal, D. P. *et al.* Photo-thermal tumor ablation in mice using near infrared-absorbing nanoparticles. *Cancer Lett.* **209**, 171–176 (2004).
4. Cole, J. R. *et al.* Photothermal efficiencies of nanoshells and nanorods for clinical therapeutic applications. *J. Phys. Chem. C.* **113**, 12090–12095 (2009).
5. Hutter, E. *et al.* Microglial response to gold nanoparticles. *ACS Nano* **4**, 2595–2606 (2010).
6. Hirsch, L. R. *et al.* Nanoshell-mediated near-infrared thermal therapy of tumors under magnetic resonance guidance. *Proc. Natl. Acad. Sci.* **100**, 13549–13554 (2003).
7. Loo, C. *et al.* Nanoshell-enabled photonics-based imaging and therapy of cancer. *Technol. Cancer Res. Treat.* **3**, 33–40 (2004).
8. Gabin, A. M. *et al.* Near-infrared resonant nanoshells for combined optical imaging and photothermal cancer therapy. *Nano Lett.* **7**, 1929–1934 (2007).
9. Skirtach, A. G. *et al.* Nanorods as wavelength-selective absorption centers in the visible and near-infrared regions of the electromagnetic spectrum. *Adv. Mater.* **20**, 506–510 (2008).
10. Melancon, M. P., Zhou, M. & Li, C. Cancer theranostics with near-infrared light-activatable multimodal nanoparticles. *Acc. Chem. Res.* **44**, 947–956 (2011).
11. Tsai, M. F. *et al.* Au Nanorod design as light-absorber in the first and second biological near-infrared windows for in vivo photothermal therapy. *ACS Nano* **7**, 5330–5342 (2013).
12. Picardi, G., Colas, F. J., Gillibert, R. & de la Chapelle, M. L. Spectral shift of the plasmon resonance between the optical extinction and absorption of gold and aluminum nanodisks. *J. Phys. Chem. C.* **120**, 26025–26033 (2016).
13. Moustaoui, H. *et al.* Shape and size effect on photothermal heat elevation of gold nanoparticles: Absorption coefficient experimental measurement of spherical and urchin-shaped gold nanoparticles. *J. Phys. Chem. C.* **123**, 17548–17554 (2019).
14. Kimling, J. *et al.* Turkevich method for gold nanoparticle synthesis revisited. *J. Phys. Chem. B.* **110**, 15700–15707 (2006).
15. Mishra, A. *et al.* Optical properties in nanofluids of gold nanoparticles in poly(vinylpyrrolidone). *J. Nanosci. Nanotechnol.* **9**, 4342–4347 (2009).
16. Alexandridis, P. Gold nanoparticle synthesis, morphology control, and stabilization facilitated by functional polymers. *Chem. Eng. Technol.* **34**, 15–28 (2011).
17. Ram, S. & Fecht, H. J. Modulating up-energy transfer and violet-blue light emission in gold nanoparticles with surface adsorption of poly(vinyl pyrrolidone) molecules. *J. Phys. Chem. C.* **115**, 7817–7828 (2011).
18. Susrutha, B., Ram, S. & Tyagi, A. K. Effects of gold nanoparticles on rheology of nanofluids containing poly(vinylidene fluoride) molecules. *J. Nanofluids.* **1**, 120–127 (2013).
19. Alrahili, M. *et al.* Morphology dependence in photothermal heating of gold nanomaterials with near-infrared laser. *J. Phys. Chem. C.* **124**, 4755–4763 (2020).
20. Cho, E. C. *et al.* Measuring the optical absorption cross sections of Au-Ag nanocages and Au nanorods by photoacoustic imaging. *J. Phys. Chem. C.* **113**, 9023–9028 (2009).
21. Mie, G. Beiträge Zur Optik Trüber Medien, Speziell Kolloidaler Metallösungen. *Ann. Phys.* **330**, 377–445 (1908).
22. Draine, B. T. & Flatau, P. J. Discrete-dipole approximation for scattering calculations. *J. Opt. Soc. Am.* **11**, 1491–1499 (1994).
23. Chen, H. *et al.* Understanding the photothermal conversion efficiency of gold nanocrystals. *Small* **6**, 2272–2280 (2010).
24. Van de Broek, B. *et al.* Specific cell targeting with nanobody conjugated branched gold nanoparticles for photothermal therapy. *ACS Nano* **5**, 4319–4328 (2011).
25. Pu, Y. *et al.* Elucidating the growth mechanism of plasmonic gold nanostars with tunable optical and photothermal properties. *Inorg. Chem.* **57**, 8599–8607 (2018).
26. Jauffred, L. *et al.* Plasmonic heating of nanostructures. *Chem. Rev.* **119**, 8087–8130 (2019).
27. Baffou, G. & Quidant, R. Thermo-plasmonics: Using metallic nanostructures as nano-sources of heat. *Laser Photonics Rev.* **7**, 171–187 (2013).
28. Jain, P. K., Lee, K. S., El-Sayed, I. H. & El-Sayed, M. A. Calculated absorption and scattering properties of gold nanoparticles of different size, shape, and composition: Applications in biological imaging and biomedicine. *J. Phys. Chem. B.* **110**, 7238–7248 (2006).

29. He, G. S. *et al.* Scattering and absorption cross-section spectral measurements of gold nanorods in water. *J. Phys. Chem. C.* **114**, 2853–2858 (2010).
30. Baffou, G., Quidant, R. & García De Abajo, F. J. Nanoscale control of optical heating in complex plasmonic systems. *ACS Nano* **4**, 709–716 (2010).
31. Richardson, H. H. *et al.* Experimental and theoretical studies of light-to-heat conversion and collective heating effects in metal nanoparticle solutions. *Nano Lett.* **9**, 1139–1146 (2009).
32. Jiang, K., Smith, D. A. & Pinchuk, A. Size-dependent photothermal conversion efficiencies of plasmonically heated gold nanoparticles. *J. Phys. Chem. C.* **117**, 27073–27080 (2013).
33. Lu, L., Ai, K. & Ozaki, Y. Environmentally friendly synthesis of highly monodisperse biocompatible gold nanoparticles with urchin-like shape. *Langmuir* **24**, 1058–1063 (2008).
34. Yu, K., Kelly, K. L., Sakai, N. & Tatsuma, T. Morphologies and surface plasmon resonance properties of monodisperse bumpy gold nanoparticles. *Langmuir* **24**, 5849–5854 (2008).

Acknowledgements

This study was supported in part by the BioFrontiers Center at the University of Colorado Colorado Springs and Chromatic Technologies Inc (CTI). The authors would like to thank Ruizheng Wang of Lahjavida for supplying the AuNPC materials. The authors appreciate Tahira Ahmad for her assistance. Mazen Alrahili would like to thank Taibah University for funding his scholarship.

Author contributions

All authors discussed the organization and content of the manuscripts. M.A. designed the experiment, took the measurements, and wrote the main manuscript. V.S. took the measurements and revised the manuscript. K.M. designed the experiment and revised the manuscript. A.P. supervised the work, critically reviewed, and revised the main manuscript.

Competing interests

The authors declare no competing interests.

Additional information

Supplementary information is available for this paper at https://doi.org/10.1038/s41598-020-75895-9.

Correspondence and requests for materials should be addressed to M.A.

Reprints and permissions information is available at www.nature.com/reprints.

Publisher's note Springer Nature remains neutral with regard to jurisdictional claims in published maps and institutional affiliations.